# Current Improvement for a 3$\phi$ Bi-directional Inverter with Wide Inductance Variation

T.-F. Wu, L.-C. Lin, C.-H. Chang, Y.-L. Lin, and Y.-R. Chang*

Elegant Power Application Research Center (EPARC)
Department of Electrical Engineering
National Chung Cheng University
Ming-Hsiung, Chia-Yi 62102, Taiwan, ROC
Email: ieetfwu@ccu.edu.tw
Tel: 886-5-2428159; Fax: 886-5-2720862

*Engineering Division
Institute of Nuclear Energy Research (INER)
Atomic Energy Council, Executive Yuan
Longtan, Taoyuan 32546, Taiwan, ROC
E-mail: raymond@iner.gov.tw
Tel: 886-3-4711400#3678; Fax: 886-3-4711064

***Abstract*-- This paper presents current improvement for a 3$\phi$ bi-directional inverter with wide inductance variation. A bi-directional inverter fulfilling grid connection and rectification with power factor correction has been designed and implemented in the laboratory. With a digital predictive current control, the inverter can accommodate wide inductance variation, improving current distortion in high power applications significantly. However, under low current levels, inductor currents have serious distortion. To improve current distortion, this paper presents four attempts, including mid-point current sampling, smooth region transition, current interleaving, and duty splitting. Theoretical analysis and experimental results are presented to verify the discussion.**

***Index Terms*-- three-phase, bi-directional inverter, predictive current control, current interleaving and duty splitting.**

## I. Introduction

Renewable power generation systems grow rapidly. By nature, renewable power is not continuous and reliable. It will be converted into dc form and buffered with energy storage elements. This brings opportunities for electric appliance and equipment which are mostly supplied with dc voltage sources. However, the distributed generation systems require bi-directional inverters to control the power flow between dc bus and ac grid, and to regulate the dc bus to a certain range of voltages [1]. The overall system configuration is shown in Fig. 1.

The bi-directional three phase inverters with grid connection (GC) and rectification (with power factor correction (PFC)) modes have been widely studied. The major concerns of an inverter design include component selection [2]-[4], control scheme [5]-[7] and soft-switching topology [8]. Component selection is always a primary task in the growing demand for higher efficiency and smaller size, especially in high power applications. The others are also important issues for achieving fast dynamics, low current distortion and low EMI. However, inductance varying with current has not been considered in controller design yet, which will result in poor stability at high power applications. In the previous research, a digital predictive current controlled 10 kW 3$\phi$ bi-directional inverter with wide inductance variation has been designed and implemented [9], which insures low total harmonic current distortion (THD < 3%) for the power levels higher than 3 kW. However, the current distortion becomes serious (THD > 10%) when the system is operated below 1 kW power rating. The current distortion especially under low current levels will affect power quality at ac grid, and this issue was seldom discussed.

This paper presents four improvement attempts. First, this paper presents how to sample current signals to insure sinusoidal inductor current even under low current levels. Secondly, smooth region transition is considered in the programming for improving current distortion at zero-crossing point of each phase. Thirdly, a current interleaving scheme is introduced to reduce peak current ripple. The last one, duty splitting approach, can reduce the current displacement at current zero crossing. In this paper, theoretical analysis of the above four improvement attempts are presented, and experimental results from a 10 kW 3$\phi$ bi-directional inverter are also presented to verify the analysis and discussion.

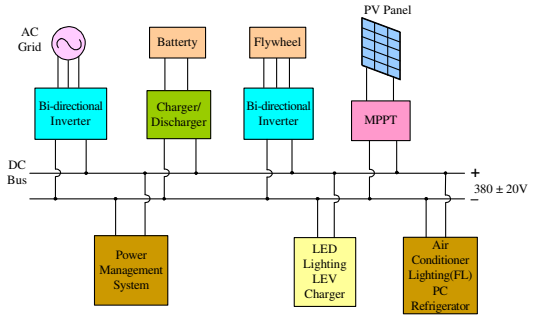


Fig. 1. Block diagram of a dc-distributed system with grid connection.

## II. Predictive Current Control

The power circuit diagram of a three-phase six-switch bi-directional inverter is shown in Fig. 2. With wide inductance variation, inverter system would be unstable,



978-1-61284-957-7/11/$26.00 ©2011 IEEE

especially in high current applications. This paper presents a predictive digital control by taking into account the wide inductance variation to overcome the problem. From Kirchhoff's Current Law (KCL), the three-phase currents satisfy the following equation:

$$i_R + i_S + i_T = 0, \tag{1}$$

where current $i_R$, $i_S$ and $i_T$ are the inductor currents shown in Fig. 2. The differential form of (1) can be written as:

$$\frac{di_R}{dt} + \frac{di_S}{dt} + \frac{di_T}{dt} = 0. \tag{2}$$

Without considering inductance variation, the three phase inductances are treated as constant, and the following equation derived from (2) will hold:

$$L_R \frac{di_R}{dt} + L_S \frac{di_S}{dt} + L_T \frac{di_T}{dt} = 0. \tag{3}$$

However, equation (3) is no longer valid for a 3$\phi$ inverter of which its inductance varies with current widely. The proposed predictive digital control laws are derived based on (1), (2) and the state equations of the inverter, and they can adapt to wide inductance variation. In the following, the control laws for the inverter operated in grid-connection (GC) mode and rectification mode are derived and presented.

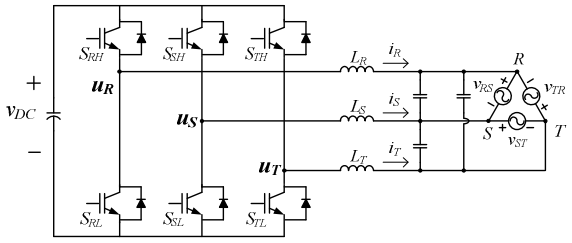

Fig. 2. Circuit diagram of a three-phase bi-directional inverter.

### A. Grid Connection Mode

The state equations of a 3$\phi$ inverter can be described as

$$u_R - L_R \frac{di_R}{dt} - v_{RS} + L_S \frac{di_S}{dt} - u_S = 0 \tag{4}$$

and

$$u_T - L_T \frac{di_T}{dt} + v_{ST} + L_S \frac{di_S}{dt} - u_S = 0, \tag{5}$$

where $u_R$, $u_S$, and $u_T$ stand for the switch voltages which change with the states of the switches. The above state equations can be also expressed in a matrix form, which is shown as follows:

$$\begin{bmatrix} u_{RS} \\ u_{ST} \end{bmatrix} = \begin{bmatrix} L_R & -L_S \\ L_T & L_S + L_T \end{bmatrix} \begin{bmatrix} \frac{di_R}{dt} \\ \frac{di_S}{dt} \end{bmatrix} + \begin{bmatrix} v_{RS} \\ v_{ST} \end{bmatrix} \tag{6}$$

where

$$u_{RS} = u_R - u_S$$

and

$$u_{ST} = u_S - u_T.$$

In the control, one line period is divided into six regions according to the zero-crossing points of the line currents, as shown in Fig. 3. In region 0°~60°, the gate driving signals can be determined from switching voltages $u_{RS}$, $u_{ST}$, and $u_{TR}$, and their corresponding switching sequence is shown in Fig. 4. In Fig. 4, "0" and "1" denote lower arm and upper arm switching, respectively. The switching sequence consists of three time intervals: $T_0$ (000 and 111), $T_1$ (100), and $T_2$ (101), which have their corresponding states of switching voltages. Thus, according to the states of $u_R$, $u_S$, and $u_T$ in region 0°~60°, equation (6) can be expressed in three different matrixes which are corresponding to three time intervals $T_0$, $T_1$, and $T_2$.

*Interval $T_0$*:

$$\begin{bmatrix} 0 \\ 0 \end{bmatrix} = \begin{bmatrix} L_R & -L_S \\ L_T & L_S + L_T \end{bmatrix} \begin{bmatrix} \Delta i_{v(R),0} \\ \Delta i_{v(S),0} \end{bmatrix} \frac{1}{T_0} + \begin{bmatrix} v_{RS} \\ v_{ST} \end{bmatrix}$$

*Interval $T_1$*:

$$\begin{bmatrix} v_{DC} \\ 0 \end{bmatrix} = \begin{bmatrix} L_R & -L_S \\ L_T & L_S + L_T \end{bmatrix} \begin{bmatrix} \Delta i_{v(R),1} \\ \Delta i_{v(S),1} \end{bmatrix} \frac{1}{T_1} + \begin{bmatrix} v_{RS} \\ v_{ST} \end{bmatrix}$$

*Interval $T_2$*:

$$\begin{bmatrix} v_{DC} \\ -v_{DC} \end{bmatrix} = \begin{bmatrix} L_R & -L_S \\ L_T & L_S + L_T \end{bmatrix} \begin{bmatrix} \Delta i_{v(R),2} \\ \Delta i_{v(S),2} \end{bmatrix} \frac{1}{T_2} + \begin{bmatrix} v_{RS} \\ v_{ST} \end{bmatrix} \tag{7}$$

where

$$T_0 = T - T_1 - T_2,$$

$T$ is the switching period, $v_{RS}$ and $v_{ST}$ are the ac grid line-to-line voltages, $v_{DC}$ is the dc-bus voltage, and $\Delta i_{v(\bullet)}$ is the variation of inductor current $i_R$ ,$i_S$ or $i_T$ in each time interval. The predictive current control includes predictive current variation $i_{v(\cdot)}$ ($=I_{ref}(n+1)-I_{ref}(n)$) to determine the control law, as shown in Fig. 5, and the final duty ratio (control) is determined based on predictive current variation $i_{v(\cdot)}$ and compensated current error $G_c.i_e$ ($=I_{ref}(n)-i_{fb}(n)$), where $G_c$ is the current error compensator. The overall control block diagram is shown in Fig. 6.

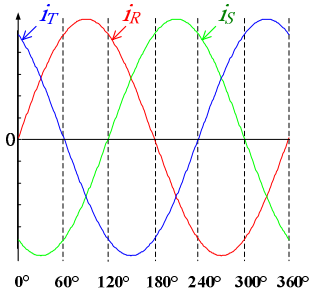

Fig. 3. Six regions in one line period divided according to the zero-crossing points of line currents $i_R$, $i_S$ and $i_T$.

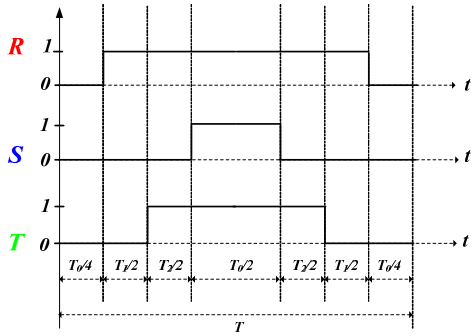


Fig. 4. Switching Sequence in Region 0°~60°.

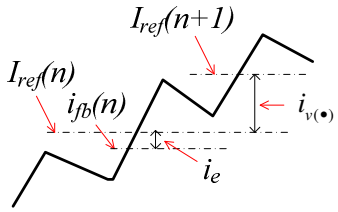


Fig. 5. Illustration of inductor current $i_L$ varying with time.

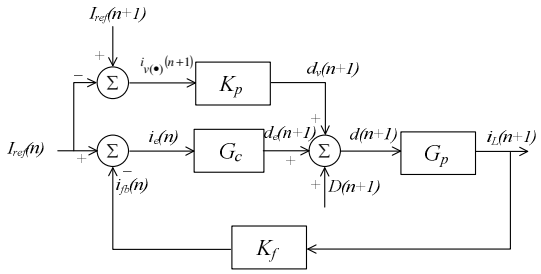


Fig. 6. A block diagram of the proposed predictive current control.

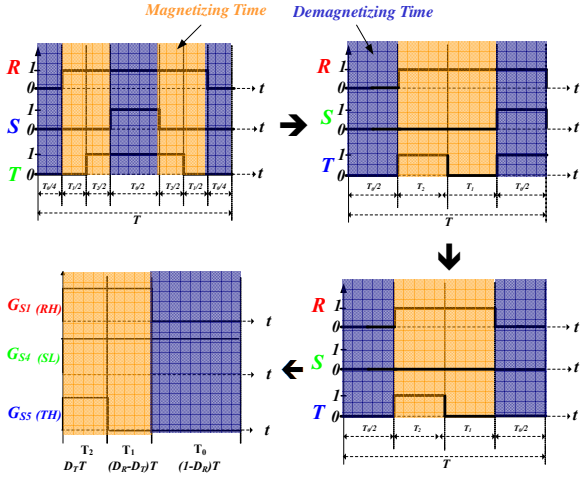


Fig, 7. The equivalent switching sequence for two-phase modulation in region 0°~60°.

Therefore, to obtain the whole inductor current variation over one switching period $T$, the current variation in each time interval should be expressed as follows:

*Interval $T_0$*:

$$\begin{bmatrix}\Delta i_{v(R),0}\\ \Delta i_{v(S),0}\end{bmatrix}=-\begin{bmatrix}\frac{L_S+L_T}{L_{total}^2} & \frac{L_S}{L_{total}^2}\\ \frac{-L_T}{L_{total}^2} & \frac{L_R}{L_{total}^2}\end{bmatrix}\begin{bmatrix}v_{RS}\\ v_{ST}\end{bmatrix}T_0$$

*Interval $T_1$*:

$$\begin{bmatrix}\Delta i_{v(R),1}\\ \Delta i_{v(S),1}\end{bmatrix}=-\begin{bmatrix}\frac{L_S+L_T}{L_{total}^2} & \frac{L_S}{L_{total}^2}\\ \frac{-L_T}{L_{total}^2} & \frac{L_R}{L_{total}^2}\end{bmatrix}\begin{bmatrix}v_{RS}\\ v_{ST}\end{bmatrix}T_1-\begin{bmatrix}\frac{L_S+L_T}{L_{total}^2} & \frac{L_S}{L_{total}^2}\\ \frac{-L_T}{L_{total}^2} & \frac{L_R}{L_{total}^2}\end{bmatrix}\begin{bmatrix}-v_{DC}\\ 0\end{bmatrix}T_1$$

*Interval $T_2$*:

$$\begin{bmatrix}\Delta i_{v(R),2}\\ \Delta i_{v(S),2}\end{bmatrix}=-\begin{bmatrix}\frac{L_S+L_T}{L_{total}^2} & \frac{L_S}{L_{total}^2}\\ \frac{-L_T}{L_{total}^2} & \frac{L_R}{L_{total}^2}\end{bmatrix}\begin{bmatrix}v_{RS}\\ v_{ST}\end{bmatrix}T_2-\begin{bmatrix}\frac{L_S+L_T}{L_{total}^2} & \frac{L_S}{L_{total}^2}\\ \frac{-L_T}{L_{total}^2} & \frac{L_R}{L_{total}^2}\end{bmatrix}\begin{bmatrix}-v_{DC}\\ v_{DC}\end{bmatrix}T_2 \quad (8)$$

where

$$L_{total}^2=L_RL_S+L_SL_T+L_TL_R\,.$$

By summarizing the above three state equations, we can have

$$\begin{bmatrix}\Delta i_{v(R)}\\ \Delta i_{v(S)}\end{bmatrix}=-\begin{bmatrix}\frac{L_S+L_T}{L_{total}^2} & \frac{L_S}{L_{total}^2}\\ \frac{-L_T}{L_{total}^2} & \frac{L_R}{L_{total}^2}\end{bmatrix}\begin{bmatrix}v_{RS}\\ v_{ST}\end{bmatrix}T-\begin{bmatrix}\frac{L_S+L_T}{L_{total}^2} & \frac{L_S}{L_{total}^2}\\ \frac{-L_T}{L_{total}^2} & \frac{L_R}{L_{total}^2}\end{bmatrix}\begin{bmatrix}-v_{DC} & -v_{DC}\\ 0 & v_{DC}\end{bmatrix}\begin{bmatrix}T_1\\ T_2\end{bmatrix} \quad (9)$$

where

$$\Delta i_{v(R)}=\Delta i_{v(R),0}+\Delta i_{v(R),1}+\Delta i_{v(R),2}$$

and

$$\Delta i_{v(S)}=\Delta i_{v(S),0}+\Delta i_{v(S),1}+\Delta i_{v(S),2}\,.$$

From (9), the time intervals of $T_1$ and $T_2$ can be determined as:

$$\begin{bmatrix}T_1\\ T_2\end{bmatrix}=\begin{bmatrix}-\frac{1}{v_{DC}} & -\frac{1}{v_{DC}}\\ 0 & \frac{1}{v_{DC}}\end{bmatrix}\left\{\begin{bmatrix}L_R & -L_S\\ L_T & L_S+L_T\end{bmatrix}\begin{bmatrix}-\Delta i_{v(R)}\\ -\Delta i_{v(S)}\end{bmatrix}-\begin{bmatrix}v_{RS}\\ v_{ST}\end{bmatrix}T\right\}$$

$$=\begin{bmatrix}-\frac{1}{v_{DC}} & -\frac{1}{v_{DC}}\\ 0 & \frac{1}{v_{DC}}\end{bmatrix}\begin{bmatrix}-L_R\Delta i_{v(R)}+L_S\Delta i_{v(S)}-v_{RS}T\\ -L_T\Delta i_{v(R)}-(L_S+L_T)\Delta i_{v(S)}-v_{ST}T\end{bmatrix}$$

$$=\begin{bmatrix}\frac{(L_R+L_T)\Delta i_{v(R)}+L_T\Delta i_{v(S)}}{v_{DC}}-\frac{v_{TR}}{v_{DC}}T\\ \frac{L_S\Delta i_{v(R)}+(L_S+L_T)\Delta i_{v(T)}}{v_{DC}}-\frac{v_{ST}}{v_{DC}}T\end{bmatrix} \quad (10)$$

Moreover, the predictive current control can be realized with a two-phase modulation. The derivation based on the concept of magnetizing and demagnetizing is shown in Fig. 7. First, vector 111 can be replaced with vector 000, because both vectors 000 and 111 stand for

demagnetizing manner, which does not affect the original operation. Secondly, in region 0°~60°, inductor currents of phases R and T can flow through the lower-arm diodes for demagnetizing; that is, for vector 000, the lower-arm switches can be turned off. Therefore, the upper-arm switch of phase S and the lower-arm switches of phases R and T can be turned off, and the lower-arm switch of phase S can be turned on all the time during region 0°~60°. The control law (duty ratio) for the two-phase modulation can be then determined as:

$$\begin{bmatrix} D_{RH} \\ D_{SL} \\ D_{TH} \end{bmatrix} = \begin{bmatrix} \dfrac{(L_R + L_S)\Delta i_{v(R)} + L_S \Delta i_{v(T)}}{v_{DC} T} \\ 0 \\ \dfrac{(L_T + L_S)\Delta i_{v(T)} + L_S \Delta i_{v(R)}}{v_{DC} T} \end{bmatrix} + \begin{bmatrix} \dfrac{v_{RS}}{v_{DC}} \\ 1 \\ -\dfrac{v_{ST}}{v_{DC}} \end{bmatrix} \tag{11}$$

where

$$D_{TH} = \frac{T_2}{T},$$

$$D_{RH} = \frac{T_1}{T} + \frac{T_2}{T},$$

and $D_{RL}$, $R_{SH}$, and $D_{TL}$ are set to zero. The duty ratios in the other regions can be also derived with the same procedure. Additionally, it can be observed that each control law or duty ratio has two inductance variables. In other words, inductance variation has been taken into account by the controller to tune the duty ratios cycle by cycle corresponding to different current levels. Thus, the control laws shown in (10) can handle wide inductance variation.

### *B. Rectification Mode*

When the bi-directional inverter is operated in rectification mode with power factor correction, the inverter acts like a boost converter which is just the complementary operation of a buck converter in grid-connection mode. Thus, again based on the two-phase modulation, the control laws in region 0°~60° for the rectification mode can be readily derived from (10) as follows:

$$\overline{\begin{bmatrix} D_{RH} \\ D_{SL} \\ D_{TH} \end{bmatrix}} = \left\{ \begin{bmatrix} \dfrac{(L_R + L_S)\Delta i_{v(R)} + L_S \Delta i_{v(T)}}{v_{DC} T} \\ 0 \\ \dfrac{(L_T + L_S)\Delta i_{v(T)} + L_S \Delta i_{v(R)}}{v_{DC} T} \end{bmatrix} + \begin{bmatrix} \left(\dfrac{v_{RS}}{v_{DC}}\right) \\ 1 \\ \left(-\dfrac{v_{ST}}{v_{DC}}\right) \end{bmatrix} \right\} \tag{12}$$

Thus, equation (12) can be re-written as

$$\begin{bmatrix} \overline{D_{RH}} \\ \overline{D_{SL}} \\ \overline{D_{TH}} \end{bmatrix} = \begin{bmatrix} 1 \\ 1 \\ 1 \end{bmatrix} - \left( \begin{bmatrix} \dfrac{(L_R + L_S)\Delta i_{v(R)} + L_S \Delta i_{v(T)}}{v_{DC} T} \\ 0 \\ \dfrac{(L_T + L_S)\Delta i_{v(T)} + L_S \Delta i_{v(R)}}{v_{DC} T} \end{bmatrix} + \begin{bmatrix} \left(\dfrac{v_{RS}}{v_{DC}}\right) \\ 1 \\ \left(-\dfrac{v_{ST}}{v_{DC}}\right) \end{bmatrix} \right) \tag{13}$$

Or,

$$\begin{bmatrix} D_{RL} \\ D_{SH} \\ D_{TL} \end{bmatrix} = -\begin{bmatrix} \dfrac{(L_R + L_S)\Delta i_{v(R)} + L_S \Delta i_{v(T)}}{v_{DC} T} \\ 0 \\ \dfrac{(L_T + L_S)\Delta i_{v(T)} + L_S \Delta i_{v(R)}}{v_{DC} T} \end{bmatrix} + \begin{bmatrix} 1 - \dfrac{v_{RS}}{v_{DC}} \\ 0 \\ 1 + \dfrac{v_{ST}}{v_{DC}} \end{bmatrix} \tag{14}$$

In the above equations, $D_{\bullet H}$ and $D_{\bullet L}$ denote the duty ratios of the upper arm and the lower arm, respectively, and $\overline{D}_{\bullet H} = D_{\bullet L}$.

## III. Current Distortion Improvement

A system diagram of the discussed three-phase bi-directional inverter is shown in Fig. 8. It can fit to both delta-connected and Y-connected ac grid. In the designed prototype, Renesas micro-chip RX62T is adopted for realizing the system controller, which has 1.65 MIPS and includes floating calculation and division. By considering wide inductance variation, the inverter can be operated stably, especially in high current applications. However, distortion improvement at low current levels is still a challenging task. Thus, this paper presents four attempts: mid-point current sampling, smooth region transition, current interleaving for reducing peak current ripple, and duty splitting for reducing current displacement at zero crossing.

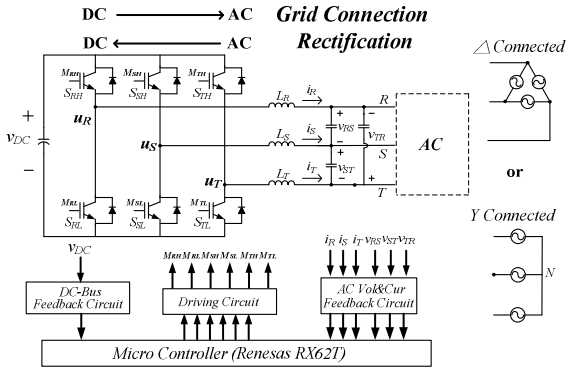


Fig. 8. System Diagram of the proposed three-phase bi-directional inverter.

### *A. Mid-Point Current Sampling*

An accurate current sampling is always a key to insure that the average value of current feedback $i_{fb}$ can match reference current $I_{ref}$ precisely. This paper presents a mid-point current sampling approach to sample induction current once at a switching cycle, as illustrated in Fig. 9. It can be seen that the pulse-width-modulation (PWM) counter is symmetrically operated. When the PWM counter counts up to the middle point (mid-point), it will trigger Analog-to-Digital (A/D) sampling and conversion, which can ensure always sampling the average value of inductor current $i_L$ over one switching period. Thus, only one current feedback value can match the reference current. Moreover, it can also avoid turn-on and turn-off switching noise.

### B. Smooth Region Transition

In the previous research, current distortions always happen at the six region transitions. These distortions become more significant, especially, at low current levels. The primary cause is that the PWM signal is turned off earlier than the desired time duration, as shown in Fig. 10. In Fig. 10, all A/D samplings and conversions occur at the crest of the PWM carrier signal. It will trigger an A/D interrupt and enter the interrupt service routine to determine duty ratios (control laws), when the last A/D conversion is finished. The CPU operation speed is very fast, and it takes around 10 $\mu s$ to execute A/D samplings, conversions and control law determination. In Fig. 10, duty ratio is updated at the trough of the carrier, and the carrier frequency is set to 20 kHz (its period is 50 $\mu s$). That is, there are 25 $\mu s$ to execute all commands, which is much larger than the total execution time 10 $\mu s$. Therefore, with the two-phase modulation, PWM output will be turned off earlier than the desired time duration, when the region transition reaches, resulting in larger current error $i_e^*$ as denoted in Fig.10. For the next period, it will need more magnetizing time to compensate the error and cause current distortion at current zero-crossing (region transition). An improving scheme is to delay the time until the desired time duration reached, as shown in Fig. 11. Adding a time delay can smooth region transition and reduce current distortion.

### C. Current Interleaving

In Fig. 7, it is apparent that the number of switching with space-vector PWM (SVPWM) is greater than that with the two-phase modulation. That is, the switching loss of the two-phase-modulation is less than that of SVPWM, which can improve electromagnetic interference (EMI) effectively. This paper adopts the two-phase modulation being primarily due to this advantage. However, the equivalent switching frequency of SVPWM is double the original carrier frequency; that is, switching ripple resulting from SVPWM can be reduced to half that from two-phase modulation. Therefore, this paper presents a current interleaving approach to reduce switching ripple for the two-phase modulation, as shown in Fig. 12. It can be seen that the switching ripples of phases R and T from SVPWM in region 0°~60° are smaller than that from the two-phase modulation, but that of phase S from SVPWM is larger due to the inductor currents of phases R and T demagnetizing at the same time. Note that inductor current of phase S is almost close to the peak in region 0°~60°; that is, the ripple of phase S will become much larger for its low inductance under high power level, which might cause flux density saturation. The proposed current interleaving approach for the two-phase modulation can reduce the peak current ripple in any regions significantly, improving the stability especially under high power levels.

### D. Duty Spitting

In symmetric PWM, there are two schemes to produce PWM output. One is uni-duty PWM, the other is bi-duty PWM. In the previous research, the uni-duty PWM was adopted for driving switches. However, it will induce a large current displacement at current zero crossing of one phase and at region transition of the other two phases, as shown in Fig. 13. This paper presents a bi-duty PWM to reduce this current displacement. In Fig. 13, it can be observed that current displacement $i_{d,bi}$ in bi-duty PWM mode has been reduced significantly from $i_{d\text{-}uni}$ in uni-duty PWM mode.

### E. Discussion

The proposed predictive current control can accommodate wide inductance variation, which can reduce the core size of a three-phase bi-directional inverter system. Moreover, the proposed control can adapt to both SVPWM and two-phase modulation. However, there still exists one drawback with the control. The control law has one term, $D(n+1)$, and this term is a duty ratio derived from $v_{RS}/v_{DC}$ or $v_{ST}/v_{DC}$ or $v_{TR}/v_{DC}$ in next period. In fact, sampling the future values of ac voltages and dc-bus voltage for next period cannot be done at the current period. Even though there exist slight differences between the sampling values of the current period and those of the next, the system might result in instability when the ac voltage changes abruptly. Therefore, how to improve the drawbacks is an issue being worth further study.

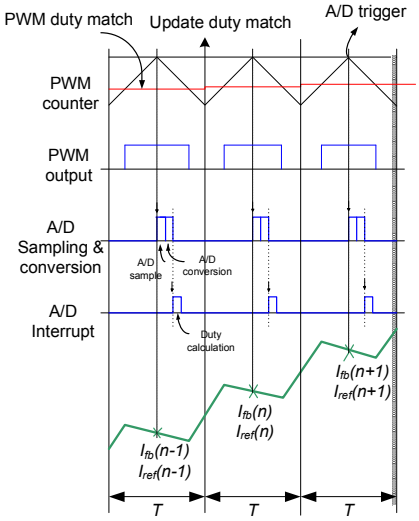


Fig. 9. Illustration of mid-point current sampling approach.

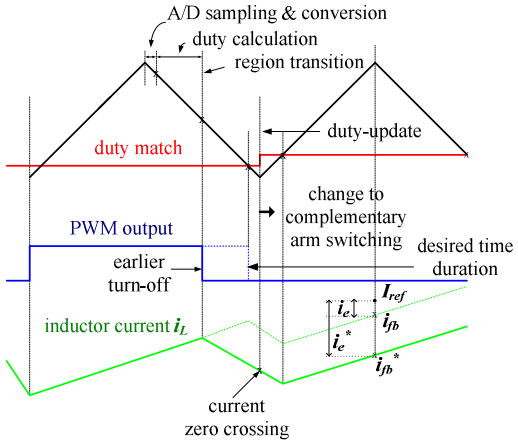


Fig. 10. Illustration of the conventional region transition.

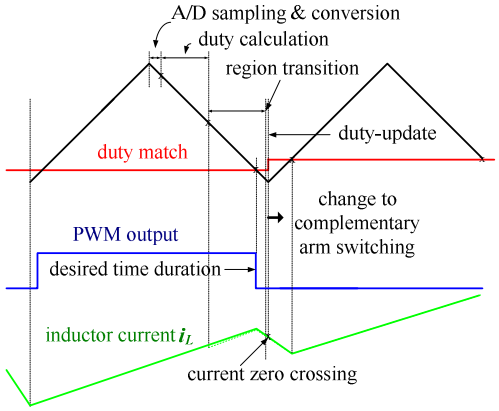


Fig. 11. Illustration of the new smooth region transition.

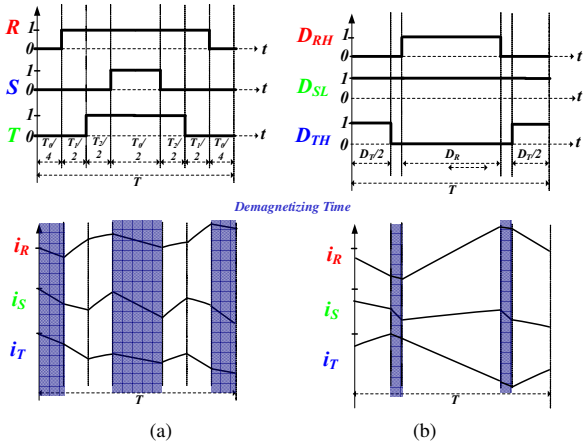


Fig. 12. Switching ripple comparison between (a) SVPWM and (b) two-phase modulation with interleaving in region 0°~60°.

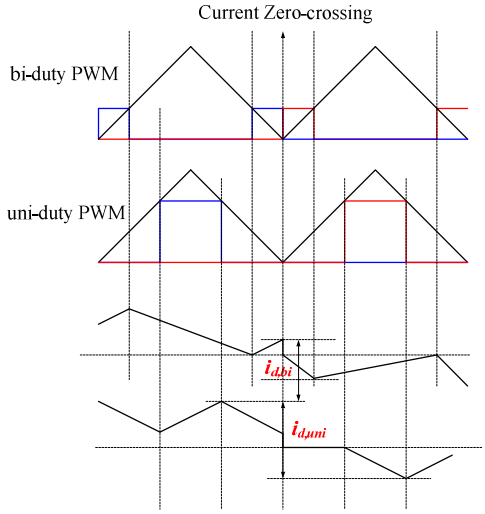


Fig. 13. Conceptual waveforms for illustrating the current displacements with uni-duty PWM and bi-duty PWM.

## IV. Experimental Results and Discussion

The proposed predictive digital control has been confirmed by a 10 kW three-phase bi-directional inverter for a dc-distribution system. For all laboratorious tests, the nominal 3$\phi$ voltage is 220 V and the frequency is 60 Hz. The inverter inductance varies from 2 mH to 300 μH per phase corresponding to 0 A to 37 A and the switching frequency is 20 kHz. The harmonic components of the output current are measured up to 20th harmonic with a power analyzer WT1600.

Figs. 14 and 15 show the current waveforms with and without considering wide inductance variation at 5 and 9 kW and with GC mode. At 5 kW, it can be seen that there is a little distortion at the peak current without considering inductance variation. However, when the inverter is operated with 9 kW, the measured inductor currents from the system without considering wide inductance variation have large distortion near the peak and a divergence in R phase.

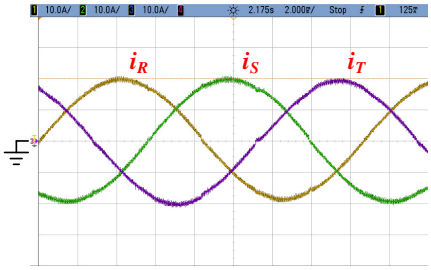


($i_R$, $i_S$ and $i_T$: 10A/div; time: 2ms/div)
(a)

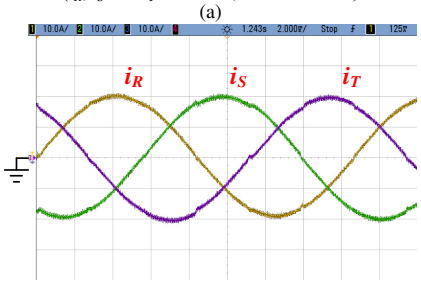


($i_R$, $i_S$ and $i_T$: 10A/div; time: 2ms/div)
(b)

Fig. 14. Measured waveforms of the three inductor currents (a) with and (b) without considering wide inductance variation (5 kW).

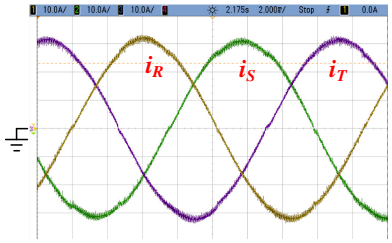


($i_R$, $i_S$ and $i_T$: 10A/div; time: 2ms/div)
(a)

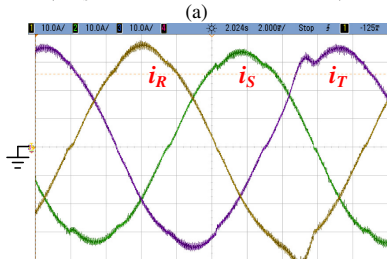


($i_R$, $i_S$ and $i_T$: 10A/div; time: 2ms/div)
(b)

Fig. 15. Measured waveforms of the three inductor currents (a) with and (b) without considering wide inductance variation (9 kW).

### A. Mid-Point Current Sampling

Fig. 16 shows the measured waveforms of the three phase inductor currents without and with mid-point current sampling at 500 W. It can be observed that the three-phase current waveforms with mid-point current sampling are smoother and they are more similar to sinusoidal waveform. Moreover, the three phase currents with the proposed approach are more uniform from each other than those without this approach.

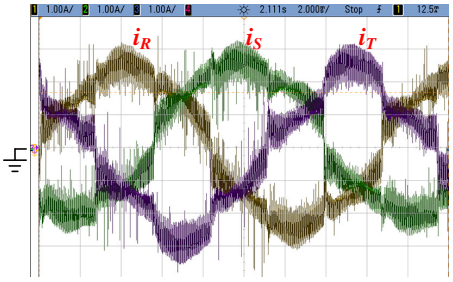


($i_R$, $i_S$ and $i_T$: 1A/div; time: 2ms/div)
(a)

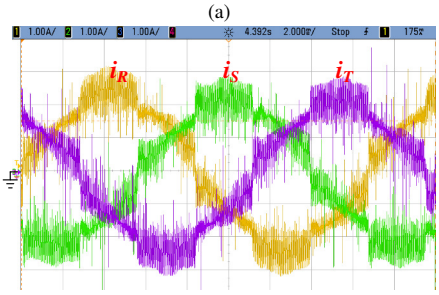


($i_R$, $i_S$ and $i_T$: 1A/div; time: 2ms/div)
(b)

Fig. 16. Measured waveforms of the three inductor currents (a) without and (b) with mid-point current sampling (500 W).

### B. Smooth Region Transition

This section does not show any improved measured current waveforms, because the current distortion at region transition results from the current displacement at current zero crossing, which is the nature response. In the above section *D*, "*Duty Splitting*", the conceptual current waveform at current zero crossing also explain the cause of the current displacement, as shown in Fig. 13. Fig. 17 shows the simulated waveform of the three phase current by MATLAB at 500 W, which verifies the theoretical analysis.

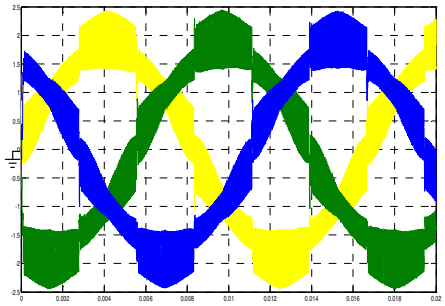

Fig. 17. Simulated waveforms of the three-phase inductor currents using MATLAB software package (500 W).

### C. Current Interleaving

Fig. 18 shows the measured waveforms of the three-phase inductor currents with and without interleaving at 800 W. It can be seen that the peak current ripple is reduced significantly with an interleaving approach, while it also increases the ripples of other phases. However, at high power rating, large peak current might cause system instability because of flux density saturation. Thus, the interleaving approach is still suitable for high power levels.

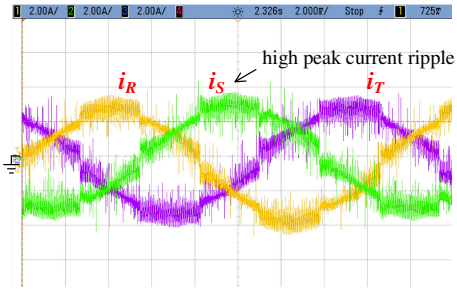


($i_R$, $i_S$ and $i_T$: 2A/div; time: 2ms/div)
(a)

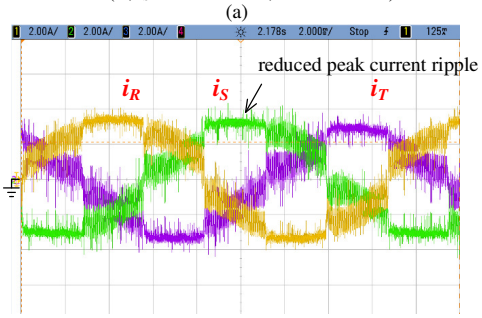


($i_R$, $i_S$ and $i_T$: 2A/div; time: 2ms/div)
(b)

Fig. 18. Measured waveforms of the three inductor currents using the two-phase modulation (a) without and (b) with interleaving in grid-connection mode at 800 W.

### D. Duty Splitting

Fig. 19 shows the measured three-phase current comparison between the inverters with a uni-duty PWM approach and a bi-duty PWM one. The current displacement of $i_{d,uni}$ and $i_{d,bi}$ are 2.3 A and 1.6 A, respectively. It is clear that the measured results can match the conceptual current displacement shown in Fig. 13. A continuous turn-on of upper- and lower- arm switches can yield a lower current displacement.

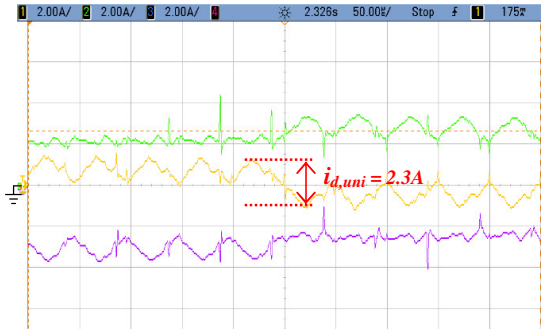


($i_R$, $i_S$ and $i_T$: 2A/div; time: 2ms/div)
(a)

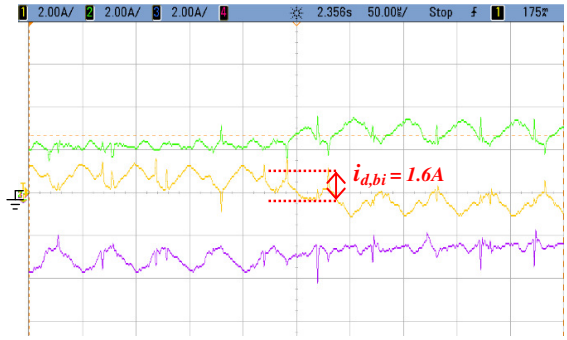


($i_R$, $i_S$ and $i_T$: 2A/div; time: 2ms/div)
(b)

Fig. 19. Measured waveforms of the three inductor currents using the two-phase modulation with (a) uni-duty PWM and (b) bi-duty PWM in grid-connection mode at 800 W.

## V. Conclusions

Current improvement for a $3\phi$ bi-directional inverter considering wide inductance variation has been presented in the paper. First, this paper has presented the predictive current control with wide inductance variation. With the control laws, the controller can tune loop gains corresponding to inductance variation cycle by cycle, which has the merit of reducing core loss and size significantly. The proposed control laws can also fit to both SVPWM and the two-phase modulation. Secondly, this paper presented four attempts to improve current distortion especially under low power level. With mid-point current sampling, the total harmonic distortion can be reduced from 10.61% to 6% at 500 W. The current interleaving approach can be adopted for high current level, because it can reduce the peak current ripple effectively. Finally, this paper has presented the duty splitting approach, bi-duty PWM, which can reduce the current displacement significantly at current zero crossing. Experimental results have verified the feasibility of the control laws and the current improvement approaches.

## Acknowledgment

The authors would like to thank the Institute of Nuclear Energy Research and National Science Council, Taiwan, ROC, for funding this research.

## References

[1]. Y. Che, Z.-G. Yang and K. W. E. Cheng, "Construction, operation and control of a Laboratory-scale microgrid," *Proceedings of 3rd International Conference on Power Electronics Systems and Applications*.

[2]. M. Rosu, X. Wu, Z. Cendes, J. Aurich and M. Hornkamp, "A Novel Electrothermal IGBT Modeling Approach for Circuit Simulation Design," in *Proc. 23rd Annu. IEEE APEC*, 2008, pp.1685–1689.

[3]. B. Ozpineci, M. S. Chinthavali, L. M. Tolbert, A. Kashyap and H. A. Mantooth, "A 55-kW Three-Phase Inverter with Si IGBTs and SiC Schottky Diodes," *IEEE Trans. on Industry Applications*, vol. 45, no 1, pp. 278-285, Jan./Feb. 2009.

[4]. R. J. Pasterczyk, J. M. Guichon, J. L. Schanen and E. Atienza, "PWM Inverter Output Filter Cost-to-Losses Tradeoff and Optimal Design," *IEEE Trans. on Industry Applications*, vol. 45, no 2, pp. 887-897, March./April. 2009.

[5]. Z. Di, V.S.S.P.K. Hari, G. Narayanan, R. Ayyanar, "Space-Vector-Based Hybrid Pulsewidth Modulation Techniques for Reduced Harmonic Distortion and Switching Loss," *IEEE Trans. on Power Electronics*, vol. 25, no. 3, pp. 760-774, 2010.

[6]. T. Ghennam, E. M. Berkouk, B. Francois, "A Novel Space-Vector Current Control Based on Neutral-Point-Clamped Inverter" *IEEE Trans. on Industrial Electronics*, vol. 57, no. 8, pp. 2669-2678, 2010.

[7]. Q. Zeng and L. Chang, "An Advanced SVPWM-Based Predictive Current Control for Three-Phase Inverters in Distribution Generation Systems," *IEEE Trans. on Industrial Electronics*, vol. 55, no. 3, pp. 1235-1246, March. 2008.

[8]. Y. P. Li, F. C. Lee and D. Boroyevich, "A Simplified Three-Phase Zero-Current-Transition Inverter with Three Auxiliary Switches," *IEEE Trans. on Power Electronics*, vol. 18, no. 3, pp. 802-813, May. 2003.

[9]. T.-F. Wu, C.-H. Chang, H.-C. Wu, J.-R. Ciou, and T.-S. Lin, "Predictive Digital Controlled Three Phase Bi-directional Inverter with wide inductance variation," in *Proc. IEEE ECCE*, 2010, pp.37–44.